Research Article Open Access

Journal of Scientific Engineering Advances

DOI: doi.org/10.63721/26JSEA0119

Development of Multispectral Polarimetric Imaging Via Drones

William H Smith[1*], Christopher J Oh[1,2], Tomas Collado[3], Yuanjian Zhang[1] and William Winston[1]

[1]Washington University in Saint Louis, Department of Earth Environmental and Planetary Science, USA
[2]Washington University in Saint Louis College of Arts and Sciences, USA
[3]Washington University in Saint Louis McKelvey School of Engineering, USA

Citation: William H Smith, Christopher J Oh, Tomas Collado, Yuanjian Zhang, William Winston (2026) Develop-ment of Multispectral Polarimetric Imaging via Drones. J. of Sci Eng Advances 2(1) 1-14. WMJ/JSEA-119

Abstract

In March and April 2024, a multispectral imaging drone was modified for multispectral polarimetric imaging (MPI) to explore its capabilities. The study targeted rooftop photovoltaic (PV) panels, examining environmental variables affecting their surfaces, and isolated trees, analyzing spectropolarimetric effects of multiple scattering in leaves before and after canopy development. Bandpass filters targeted chlorophyll absorption (~650–680 nm), red edge transition (~680–750 nm), and near-infrared reflectance plateau (~750–850 nm). One flight tested drone characteristics, while two acquired MPI data. The drone, equipped with a polarizer,was calibrated in the laboratory to normalize flight data.

Percent linear polarization (PLP) and angle of polarization (AOP) were derived for PV panels, interpreted using manufacturer specifications, and for trees with and without canopy, analyzed with standardized methods. Cloudiness during the "tree with canopy" flight introduced diffuse illumination, affecting scattering patterns, which were similar between datasets. This suggests diffuse light dominated polarization signals, necessitating further measurements.

The primary goals—modifying the drone for MPI and defining its quantitative imaging capabilities—were achieved. The platform successfully captured spectral and polarization data, advancing remote sensing for PV panel monitoring and vegetation analysis. Limitations included only two data flights and cloudiness impacting polarization measurements. Future work will address these by optimizing flight conditions and expanding datasets. This study highlights MPI's potential for material and ecological applications, emphasizing the need for robust calibration and environmental correction to ensure reliable polarimetric data.

***Corresponding author:** William H Smith, Washington University in Saint Louis, Department of Earth Environmental and Planetary Science, USA.

Research Article *Open Access*

Submitted: 31.10.2025 **Accepted:** 05.11.2025 **Published:** 06.02.2026

Keywords: MPI, Drone, Rooftop PV, Tree Canopy, Stokes Parameters

Abbreviations

MPI: Multispectral Polarimetric Imaging
PV: Photovoltaic
PLP: Percent Linear Polarization
AOP: Angle of Polarization
MSI: Multispectral Imager
MPI: Multispectral Polarimetric Imager
HBE: Hydrocarbon Base Energy
IRE: Intermittent Renewable Energy
MCS: Monocrystalline Silicon
EM: Electromagnetic
FOV: Field of View
TIFF: Tag Image File Format
MAR: Multilayer Anti-Reflection

Introduction & Objectives

A literature search shows that multispectral polarimetric imaging (hereafter, MPI) results with drones have not been published as of 2024. The impediments to MPI include the much larger data set required, the additional constraints on the measurement process and drone stability, and the limited data base for polarization effects in real world scenes. Snapshot imaging of the spectral and polarimetric variables is not feasible with existing platforms. The required serial MPI measurements can be performed using drone GPS capabilities. Here, we used a modified P4 Phantom DJI Matrice 600 Pro drone for acquisition of MPI measurements of anthropogenic and biological targets [1].

The five passbands for the P4 drone are similar to the Landsat visiblenir passbands [2]. Landsat data may be a guide for high spatial resolution (better than 30m resolution) drone MPI studies of selected targets. The polarization measurement capability, in principle, may enable more accurate determination of the PV optical response and power output versus solar insolation incidence angle in order to optimize the energy production of installed PV facilities. The addition of a wire grid linear polarizer (minimum extinction ratio 300:1 from 400nm to 900 nm) converts the multispectral imager (MSI) drone to a prototype multispectral polarimetric imager (MPI), in principle, capable of generating Stokes Parameters. We conducted measurements with the modified drone to determine the accuracy and precision of the MPI data with the drone. The most essential improvements are specified in the conclusions.

Measurement Goals

Prior ground-based studies of the Red Edge and its relationship to plant vitality, nutrient supply, drought conditions, etc. suggest that NDVI and NDRE measurements, extended to include linear polarization effects, could result in gains over MSI alone. For example, rapid changes in absorptance across the chlorophyll region are known to alter both the spectral absorption and the linear polarization, due to the scattering within leaves, in a manner dependent on and related to biological vitality, nutrient deficits, and/or the consequences of drought [3].

Net Zero 2050 is based on a transition from hydrocarbon base energy (HBE) to intermittent renewable energy (IRE). Electricity is to be produced via wind turbines and solar insolation of photovoltaic arrays. Monocrystalline silicon (MCS) is the leading material in the ongoing energy transition effort. It is a well understood, durable, cheap material available in great quantities. The maximum PV conversion efficiency of sunlight to electricity for the single junction MCS device is the Shockley and Queisser limit of 36% for MCS. MCS efficiency for the best research panels reached 24% in 1995, followed by a slow rise to just over 26% by 2015, with essentially no further improvement to 2025 [4,5].

The ultimate multijunction PV efficiency was investigated by Hirst and Ekins-Daukes who showed the limit to be just over 58%. Losses due to collection efficiency were not included and would reduce the efficiency further [6,7]. This limit is analogous to the Betz limiting efficiency for wind turbines. The best multijunction research cell (by 2025) reached 47% efficiency in a four-junction device, only 10% short of the ultimate. This research device is neither cheap nor stable compared to MCS.

Commercial grade photovoltaic (PV) panels are designed to absorb and convert sunlight to electricity at the highest feasible efficiency consistent with utility scale application. Monocrystalline silicon PV panels are fabricated with antireflection coated surfaces to maximize the transmission and conversion of solar irradiance into direct current electricity [8]. The coatings are designed to minimize Fresnel reflectance in unpolarized sunlight. The antireflection coated surfaces can, in principle, produce substantial polarization effects as a function of the irradiance incidence angle across the multispectral pass bands, measurable via MPI.

The responsivity of a utility scale PV system is always lower than the best research panels. Mass production techniques must account cost; research panels do not [9]. Measurement of the absolute efficiency of the panels we observed was not a goal of the present study, but the panels achieve ~19% efficiency, according to the manufacturer [8]. Seasonal performance has been measured, however, and is relevant to our remote sensing goals. The remaining energy is dissipated as heat to the environment by the panels, producing city-like heat islands.

Maintenance of the output of installed solar panels remains an important challenge and receives much well-deserved attention. MPI may play an important role in PV maintenance by automatic monitoring of the increasingly large PV facilities, whatever their configuration. MCS (as with other PV materials) is subject to a variety of time-dependent physical and environmental degradations. These include temperature changes (negative coefficient of ~0.5% per C degree), changes in the MCS surface properties, the degradation of transmitting surfaces and/or electrical contacts, delamination of backings, and/or loss of transmittance due to surface contamination. Physical damage can also occur from high winds, hail, ice or snow accumulation, animals grazing among the panels, etc.

PV panel prices have declined so that supporting infrastructure, e.g. inverters, inertial capacitors, grid connections and particularly, computer control facilities may be a greater expense than the PV panels. One consequence is that roof-top PV is frequently installed in physical orientations to maximize spatial coverage to achieve larger total PV area, but less efficient energy production (e.g. the Nevada Tesla Gigafactory is a prime example, as is Washington University, as described below).

Ideally, PV panels should be perpendicular to the incident solar radiance at all times, but other objectives often supersede that criterion. Tracking panels are more expensive, consume more space, and have higher maintenance costs. Output per unit (roof top) area may be maximized by the fraction of roof coverage with PV panels rather than optimizing PV panel orientation. Low-cost PV panels encourage this ‘blanketing’ approach. The effects of physical arrangement and orientation on PV output are important considerations in their overall efficiency, economy, and energy output.

In arid regions, tilted PV panels are quickly covered by dust/dirt. Vertical bifacial panels should be less susceptible [10]. Saudi studies showed that ‘dry cleaning’ via electrostatic repulsion yielded temporary improvement, but long-term degradation in output continued [11]. PV on roofs and solar facilities in California are typically washed during the dry season. The water volume and cost of the cleaning apparatus and washing are non-trivial. In addition, dust control is required by maintenance operations in large PV facilities. That, alone, consumes about 45 million gallons annually for Solar Star, CA [12]. Vertical bifacial panels would incur electrostatic and chemical adherence and certainly bird guano on both sides. Drone monitoring of PV facilities, regardless of configuration could be completely automated and efficient. MPI methods which are sensitive to surface scattering by dust/guano can, in prin-ciple, provide a simple remote sensing method for routine assessment of the operational status of PV panels in very large utility scale facilities.

To meet the Net Zero 2050 mandate to eliminate net CO2 production, PV and wind must be used everywhere feasible [5]. The replacement of ALL energy requires more than five times the IRE production than just electricity alone. The 25,000 km^2 of PV in operation in 2025 were sited on the best locations first. Today, PV is necessary in other than arid regions. Missouri, for example, has little wind resource, and must rely primarily on PV for renewable electricity. The Missouri annual average skies are clear to partly clear 55% of the time [13]. Rainfall is abundant in Missouri. Dust is less an issue than bird guano which is abundantly deposited on MO PV, affecting light transmission to the active silicon surface (see below) [14]. Dust and bird guano both have the property that the longer they remain on the PV surface, the more tightly they adhere [11]. Washington University has multiple roof PVC installations pelted by bird guano. The roof panels studied here are built by Canadian Solar [8]. The output of building roofs is routinely measured, but data for the output of individual PV panels is not available.

Spectropolarimetric Analysis; Specifying Stokes' Parameters

Maxwell's equations provide a description of the electromagnetic (EM) field. The polarization of an electromagnetic wave refers to the oscillation plane of the EM field. The four Stokes Parameters characterize any light beam [15]. Stokes Parameters may be derived from measured spectropolarimetric images. Incident sunlight can be resolved into two components, Er and El, where Er is subjected to a constant retardation, ε, with respect to El. Let I (ψ, ε) be the intensity of light due to vibrations in the direction making an angle ψ with the l direction, then:

$$I(\psi, \varepsilon) = \tfrac{1}{2}\,[I + Q\cos 2\psi + (U\cos\varepsilon + V\sin\varepsilon)\sin 2\psi],$$

where the total intensity is I, the degree of linear polarization is Q, the angle of polarization is U, and V is the degree of circular polarization. Then, Stokes' parameters are found from the following measurements, using linear polarizers and quarter-wave plates:

$I = I\,(0^{o}, 0) + I\,(90^{o}, 0) = I_l + I_r$ (= ½(I(-45^{o}) + I(0^{o}) + I(45^{o}) + I(90^{o})); for four rotational positions.)

$$Q = I(0^{o}, 0) - I(90^{o}, 0) = I_l - I_r$$
$$U = I(45^{o},0) - I(135^{o},0)$$
$$V = I(45^{o},\pi/2) - I(135^{o}, \pi/2)$$

The first parameter, I, describes the intensity of the light beam and is normalized to be equal to 1 (if the light is spectrally resolved, then each resolved spectral region is separately normalized). The second parameter, Q, describes the degree of horizontal polarization compared to vertical polarization. +1 indicates that the beam is horizontally polarized. -1 that the beam is vertically polarized. U describes the degree of 45/-45 degree polarization. +1 would state that the beam is polarized completely at 45 degrees, and vice versa. The V parameter indicates the degree of circular polarization.

If we assume that an EM wave is elliptically polarized, then we can calculate the intensity of the beam, I, by taking the sum of its x component and y component. Measurements made for the four angles with linear polarization determine the Stokes parameters I, Q, and U and characterize the light beam. Addition of a quarter wave plate would permit circular polarization to be determined. Then,

P = fractional linear polarization and φ = polarization angle are calculated from:

$P = (Q^2 + U^2)^{1/2}/I$ = polarization fraction where the sign of P is given by the sign of Q,

and

$\varphi = \tfrac{1}{2}\tan^{-1}(Q/U)$ = polarization angle in degrees. The measured and calibrated data are presented below.

Materials and Methods

Spectropolarimetric Analysis; Specifying Stokes' Parameters

Maxwell's equations provide a description of the electromagnetic (EM) field. The polarization of an electromagnetic wave refers to the oscillation plane of the EM field. The four Stokes Parameters characterize any light beam [15]. Stokes Parameters may be derived from measured spectropolarimetric images.

Incident sunlight can be resolved into two components, Er and El, where Er is subjected to a constant retardation, ε, with respect to El. Let I (ψ, ε) be the intensity of light due to vibrations in the direction making an angle ψ with the l direction, then:

$$I(\psi, \varepsilon) = \tfrac{1}{2} [I + Q \cos 2\psi + (U \cos \varepsilon + V \sin \varepsilon) \sin 2\psi],$$

where the total intensity is I, the degree of linear polarization is Q, the angle of polarization is U, and V is the degree of circular polarization. Then, Stokes' parameters are found from the following measurements, using linear polarizers and quarter-wave plates:

$I = I(0^o, 0) + I(90^o, 0) = I_l + I_r$ $(= \tfrac{1}{2}(I(-45^o) + I(0^o) + I(45^o) + I(90^o))$; for four rotational positions.)
$Q = I(0^o, 0) - I(90^o, 0) = I_l - I_r$
$U = I(45^o,0) - I(135^o,0)$
$V = I(45^o,\pi/2) - I(135^o, \pi/2)$

The first parameter, I, describes the intensity of the light beam and is normalized to be equal to 1 (if the light is spectrally resolved, then each resolved spectral region is separately normalized). The second parameter, Q, describes the degree of horizontal polarization compared to vertical polarization. +1 indicates that the beam is horizontally polarized. -1 that the beam is vertically polarized. U describes the degree of 45/-45 degree polarization. +1 would state that the beam is polarized completely at 45 degrees, and vice versa. The V parameter indicates the degree of circular polarization.

If we assume that an EM wave is elliptically polarized, then we can calculate the intensity of the beam, I, by taking the sum of its x component and y component. Measurements made for the four angles with linear polarization determine the Stokes parameters I, Q, and U and characterize the light beam. Addition of a quarter wave plate would permit circular polarization to be determined. Then, P = fractional linear polarization and φ = polarization angle are calculated from:

$P = (Q^2 + U^2)^{1/2}/I$ = polarization fraction where the sign of P is given by the sign of Q,
and $\varphi = \tfrac{1}{2} \tan^{-1} (Q/U)$ = polarization angle in degrees.

The measured and calibrated data are presented below.

Data Collection

The MPI drone was flown over Washington University in Saint Louis. Two data collection flights were allocated. Diffuse and direct solar irradiance illuminated the scene. Due to Washington University in Saint Louis policies and constraints imposed by the university police department, we had to limit our drone research area to the East End of Danforth campus or Tisch Park. We selected three sites within the park: 1) rooftop PV installations and 2) isolated trees. Data was collected at an altitude of 30 meters above ground level of the site being studied. The 30-meter height was chosen to have a field of view (FOV) of about 30x30 m, which included the PV installations and the tree canopy. A single wire grid polarizer (contrast exceeding 300:1 longwards of 400nm) was attached by a 3D printed mount and covered the six multispectral cameras of a DJI Matrice 600 Pro aerial drone. The six cameras include a Bayer RGB imaging camera, and blue, red, green, red edge, and infrared passband cameras.

In Figure 1. below, the five drone data cameras' individual pass bands are plotted over a typical chlorophyll absorption.

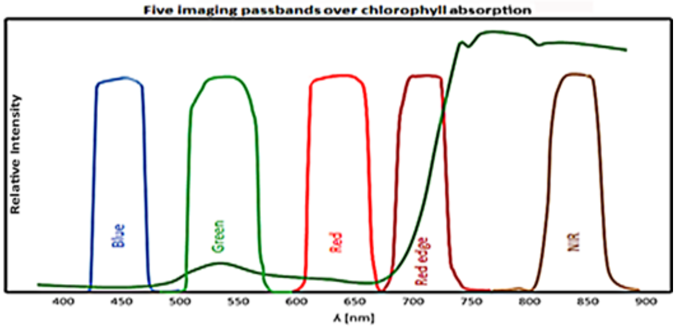

Figure 1: Multispectral Passbands Over a Chlorophyll Spectrum

At each site location, the six passband images were taken for the four position angles required for the Stokes Parameter measurement: 0°, 45°, 90°, and 135°. The mean rotation error was ~1°, based on GPS Coordinates. Data was taken for each of three sites near noon on March 21, 2024, before trees had leafed out and on April 19, 2024, after the canopy had developed. The constant altitude of the drone ensured a nearly consistent field of view across each set of photos and made inter-comparison in the data analysis simpler. At each site, for both data measurements, data were collected four times for each passband imaged by the rotated MPI drone. Thus, at each site, 24 '16 bit' digital MPI images were acquired. Each photo was then converted into an uncompressed Tag Image File Format (TIFF) file.

Data Calibration

- Multiple calibrations in a proper series are required to normalize the raw data. These include detector bias and pedestal removal, normalization of pixel-to-pixel variation and dark current. We did not correct for the simple lens distortion, although this is feasible with the drone algorithms.
- Standard reflectance panels Illuminated with tungsten-halogen and diode lamps were viewed by the drone cameras. One hundred images of each were collected and stacked to improve signal-to-noise. These form a master flat field for pixel-to-pixel normalization of all data frames.
- One hundred dark images were acquired to establish dark current and read noise at room temperature. The dark current was negligible for our exposure times.
- Javascripts (see supplementary materials) were written to create and stack master calibration images, then to remove the bias and then, to normalize pixel-to-pixel response.
- The five pass band filters were normalized via the built-in sun sensor, as per drone instructions.

To determine the S/N in the data, we required the detector specifications to determine the nominal well depth versus digitization to prevent digitization noise limitations and ensure photon noise limitations. The collected raw data were normalized as noted above. Electrons per data number were estimated. It is our conclusion that the digital camera data is described as '16-bit', but is, in fact, digitized to 12 bits with a pedestal of 4096 data numbers added. A difficulty in acquiring specific detector details from the manufacturer was incurred. The cameras are likely special models built to specification.

Calibration Steps

First, the Darkmaster is subtracted from data files and from Flatmaster to remove bias and dark current offset. The normalized Flatmaster, is a floating-point image, with a peak value 40-50,000 data numbers (DN). Each data file is divided by the Flatmaster to normalize the pixel-to-pixel variance. The data files are now 16-bit floating point images. The five pass band data files are then normalized with the sunlight sensor value. The sunlight sensor value was extracted with the XIF tool from image metadata. We selected and extracted the desired spatial regions of the PV from the corrected data files for all four drone orientations, and summed all pixels for each same area on the PV panels. Using the same PV panel areas, corrected, and normalized with the sunlight sensor, permitted extraction of Stokes Parameters, as described below.

The NIR band samples the reflectance plateau, the red edge filter senses the red edge rise and position, while red, green, and blue bands sample the strong absorption region for chlorophyll. The addition of a linear polarization measurement extends and also complicates the measurement process as described above and below. The cameras are briefly and incompletely described in [1]. Each camera is normalized as described above. The PV panels' reflectance spectrum is discussed next.

The Photovoltaic Panels

The panels, manufactured by Canadian Solar, Inc, are monocrystalline silicon panels with a multilayer anti-reflection (MAR) coating for the visible-nir spectrum. An example normal incidence spectral reflectance curve is shown below in Figure 2 [8,16].

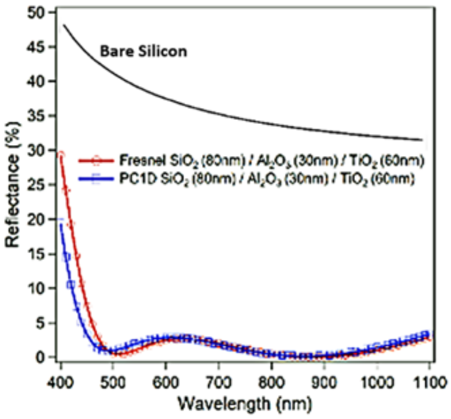

Figure 2: MAR Coating on Silicon.

Brewster's Angle for bare silicon is 75.9°. We have not been able able to obtain information on the angular dependence of reflection for the actual MAR coated silicon, so we cannot assess its exact effect. In principle, with a panel in the laboratory, we could measure the MAR angular characteristics ourselves.

The high-impact tempered front cover glass is not AR coated on either side. The Fresnel reflection of the two surfaces of the glass is ~8% at normal incidence, and increases at angles off normal. The details of the MAR coating applied to the Canadian Solar panels are not published. Given the application, we assume the MAR coating is optimized for minimal reflectivity increase off normal incidence. The drone observing geometry did not change significantly during the measurements on a given day, but changed significantly between 21 March and 19 April as sun zenith angle decreased from 39° to 28°.

The drone is equipped with an altaz gimbal mount that cannot rotate. The entire drone was rotated under GPS control to generate the four observation angles to derive the Stokes parameters. The maximum error between measurements in the data series was ~1 ° between data acquired on different dates and at 30 m above the buildings. The wind jitter depended on wind speed and veer. The data acquisition was too rapid for jitter to have any relative effect on the spatial resolution. Both data acquisition dates were selected for low wind conditions, based on day-ahead forecasts.

The effect of an angular error is given by the first derivative of Malus Law:

$$\mathbf{f' = d/d\theta\, (\cos^2 \theta) \approx -\sin (2\theta),}$$

so the intensity change, for an angular error of no more than 1° is sine (0± 2 °) and sine (45± 2°), or a ~4% maximum error in I, due to the angular error. We discuss the effect of this error in the discussion. The error would be larger for diffusely illuminated PV panels since incident diffuse illumination has a nearly hemi-spherical directional variation over which an integration should be made. We analyzed the diffusely illuminated panels in the same manner as direct illuminated panels with a similar result (below), ignoring the angular dependence. Having no opportunity to repeat our measurements, we defer detailed discussion of the diffuse scattered illumination until we have an opportunity to acquire more data.

The rotation required to derive Stokes Parameters means the overlap among rotations is incomplete due to the 1600 x 1300 pixel camera format (Figure 3).

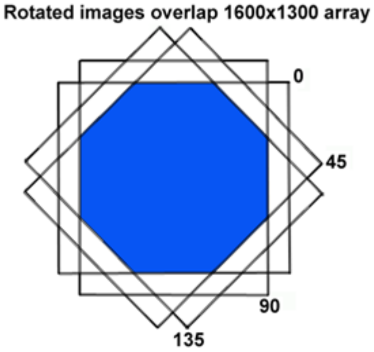

Figure 3: Overlap of Rotated Fields of View.

The pixels which are not in common in each rotated image cannot contribute to the measurement. We were able to acquire full overlap of the measured regions of interest in every rotation.

Camera Registration

The six drone cameras are not accurately bore-sighted, as can be seen in Figure 6 from the white lines imposed on the image set obtained in one frame of a test object.

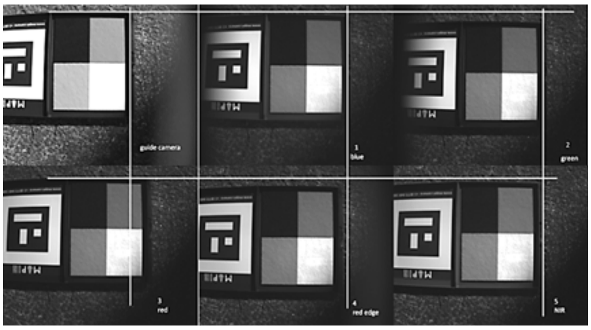

Figure 4: Simultaneous Images of Test Patterns.

Each image also has different image aberrations for each camera for each angular view. Adjustment of camera optics could remove nearly all the shift in the images, but the cameras and optics are not adjustable. Optical distortion is a correctible aberration, varying as a cubic term from the optical center, but given the measurement conditions, it was not corrected. For the preliminary study of MPI, we utilized areas as near to the center of the FOV as feasible to minimize optical distortion and normalized the signal for the regions of interest (ROI) (totaling 85,000±100 pixels each, both for direct and diffusely illuminated pixels) as a single number.

The remaining aberrations blur the spatial resolution. The single element aspheric lens in the P4 cameras could be readily improved. Since our purpose was to demonstrate MPI practice using a small drone, the optics were accepted.

Figure 5 is view of regions of interest for PV panels on the Schnuck Pavilion roof in Tisch Park (Appendix 1).

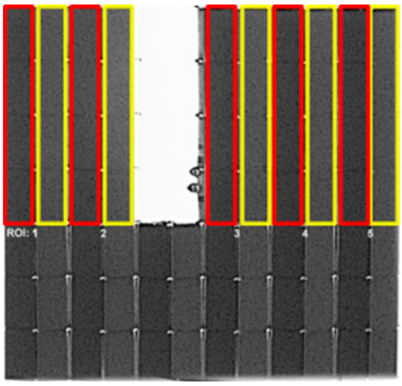

Figure 5: Schnuck Pavillion Photovoltaic Cell Regions of Interest, 19-4-2024

East tilted, directly illuminated panels are the yellow outlined regions of interest labeled ROI 1-5 on the Q, U, P, and φ graphics, below, while west tilted, red outlined regions were not illuminated directly, but by scattered light at the time of the measurement. The results of data normalization, summing, and computing Q,U,P, and φ is shown below. These areas contain 85,000 ±100 pixels as noted above.

Statistical Analysis

Due to the preliminary nature of this study, no formal statistical tests were performed. Data were analyzed descriptively to characterize the polarization properties of photovoltaic (PV) panels and tree canopies. For each site (rooftop PV panels and isolated trees) and measurement date (March 21, 2024, and April 19, 2024), the sample size (N) consisted of 24 images per site, derived from six multispectral cameras, each capturing images at four polarization angles (0°, 45°, 90°, and 135°). Regions of interest (ROIs) for PV panels and tree canopies contained 85,000 ± 100 pixels per ROI, providing a robust sample for computing Stokes Parameters (I, Q, U, V), polarization fraction (P), and polarization angle (φ).

The Stokes Parameters and derived metrics (P, φ) were calculated as mean values across all pixels in each ROI for each passband and polarization angle, as described in the Data Calibration section. The angular error in drone rotation (~1°) was quantified using the first derivative of Malus' Law, resulting in a maximum intensity error of ~4%, as detailed in the Photovoltaic Panels section. This error was considered in the interpretation of results but was not subjected to statistical testing. Results, including mean Q, U, P, and φ values, are presented in Figure 7, with sample sizes (N = 85,000 pixels per ROI, N = 24 images per site) indicated in the figure legend.

To ensure replicability, all data processing steps, including calibration and normalization, were performed using custom JavaScripts (see Supplementary Materials Appendix 1). The descriptive results provide a baseline for future studies, which may incorporate statistical comparisons (e.g., t-tests or ANOVA) to assess differences in polarization metrics between sites, dates, or illumination conditions.

Results

We derived Q and U as described above, seen in Figure 8. Q and U are similar for both diffuse and direct illumination.

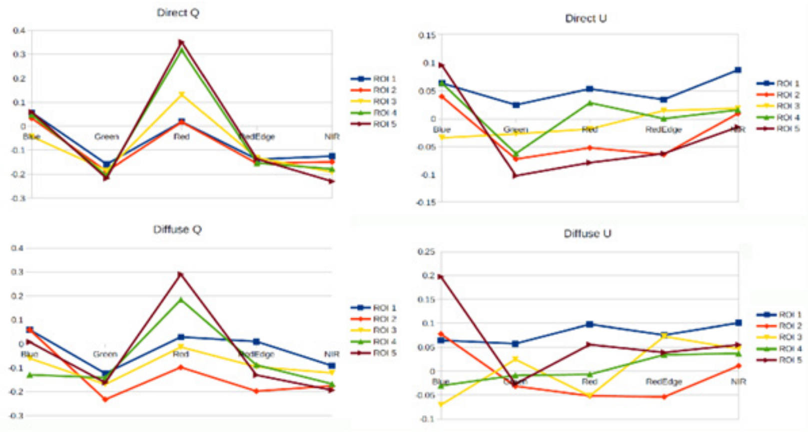

Figure 6: Data From All Measured and Normalized Regions of Interest.

Our viewing angle differs by 32° east-west due to the panel tilts. Diffuse illumination is, as expected, ~10% of the direct illumination. It also has a more blue spectral distribution, due to Rayleigh scattering. The units of Q and U are proportional to watts/m2, P is the fractional linear polarization, and φ is the angle of polarization, in degrees, extracted from the data using the formalism above. Diffusely scattered illumination necessarily alters ‘within leaf’ scattering and reduces the signal/noise due to reduced illumination.

In Figure 7, we plot the average of all direct illumination ROIs to improve the S/N.

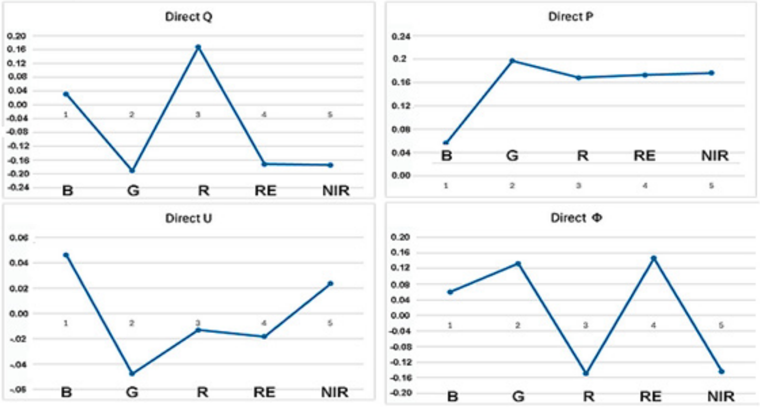

Figure 7: Summed Direct illumination for ROI 1-5.

Direct Q and U Stokes Parameters are plotted at the left of Figure 9, and to the right, corresponding, P, percent linear polarization and, φ, the polarization angle are plotted. The percent polarization is seen to be ~0% for B, 17-20% for G, R, RE, and NIR filters, while the polarization angles are all near zero, too small to discuss further until more precise measurements are acquired. The percent polarization may be significant. Only the blue filter yielded a significantly different value. The MAR coating is least effective in the blue portion of the spectrum and reflectance rises sharply in Figure 4 above. By taking data at different incident solar angles, this could be sorted out. Future measurement will include such extended measurements.

Time Dependence of Energy Production by the Solar Panels

Figure 8, from output data provided by the facilities engineering of Washington University, shows a slow decline in the energy production.

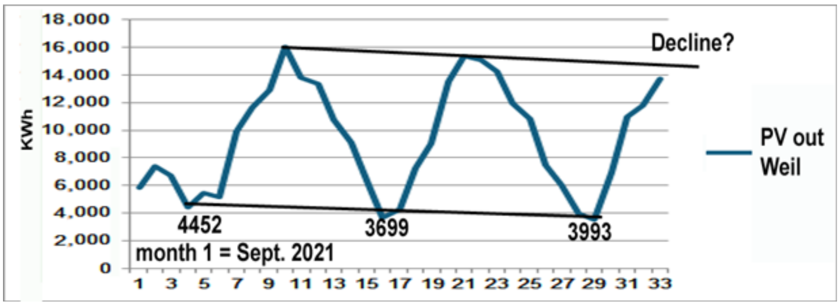

Figure 8: Thirty-three Months of PV Panels' Energy Production on Weil Hall.

MPI drone measurements can confirm and quantify the trend. There are a number of possible causes: PV aging effects such as contact changes, thermal effects, and transmission effects due to the detected bird guano, and haziness or cloudiness trends.

PV Orientation

The PV panel orientation, Figure 9, maximizes the surface coverage of the roof, but not the energy production per panel, and allows no access between panels, complicating cleaning and/or replacement.

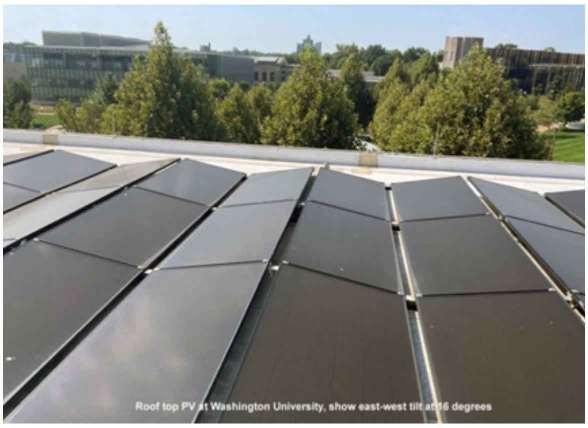
Roof top PV at Washington University, show east-west tilt at 16 degrees

Figure 9: PV Panel East-West Tilts

These panels are tilted at 16°, peak to valley east-to-west, and orientated in a north-south direction. This arrangement is common on roofs, e.g. the Tesla Nevada Gigafactory. For the highest performance, PV panels must track the sun, both in altitude and azimuth. Tracking in altitude alone results in about 25% higher per panel energy production (re: Solar Star, CA), annually, but fewer panels could be accommodated in a given roof area. For Saint Louis, the optimum angle for non-tracking PV panels would be oriented toward the south, tilted back at a 51° elevation angle. In the optimum orientation for any specific latitude, the panels are spaced so as to not shade one another at lower sun elevations. Spacing is not necessary for the east-west 16° tilt arrangement. This allows a larger fraction of a roof to be covered. For optimum orientation for non-tracked panels at the latitude of St. Louis, the seasonal variation of monthly output would be 2.25X between the summer solstice maximum and the winter solstice minimum. The measured monthly PV output, in Figure 10, varies by 4:1 seasonally or nearly twice the seasonal variation as for optimum orientation. The effects of air mass and solar foot print also should be included along with the seasonal variation, as well as the effect of aerosols. These PV panels are located in a large city with considerable and variable aerosol contamination. The slow measured annual decline in Figure 10 may have more than one contributor. This is a subject to be investigated with MPI methodology.

Bird Guano and other Residues on the PV Surface

Inspection of the roof top PV showed significant contamination primarily with bird guano residues (struvite and ammonium urate, ref 14). In Figure 12, rivulets are seen where the material is streaked by rain runoff. Newer white spots are seen as well. This material could be washed from the PV surface, but care should be taken not to abrade the glass surface to produce permanent scattering losses. These rooftop panels are not routinely washed, as panels in semiarid CA or desert Saudi Arabia are. The build-up of residues may be impacting the output as shown by the gradual decline on energy produced and might cause a greater effect near the winter solstice due to greater incidence angles. It would be a straightforward measurement to differentiate among the possible sources of output decline with our drone MPI measurement, coupled with the monthly output data.

Figure 10: Bird Guano Rain Streaks on PV Panels.

Discussion

The following points can be made from the study:

- The direct and diffuse illuminated PV panels shown a closely similar Q and U, as plotted in Figure 8. The similar result demonstrates that MPI measurements are feasible, even with a drone not designed for that purpose and illustrates the measurement error for the current measurement circumstances
- Detailed knowledge of the specifications of the CMOS arrays used, coupled with essential laboratory measurements, is required to define the S/N. The CMOS arrays for the P4 drone are apparently considered proprietary information. An analysis of similar CMOS arrays shows that a 3µm x 3µm pixel has a well fill near 10,000 electrons, represented by about 60,000 data numbers – dn, (4096 dn are a fixed pedestal), or ~6 dn/ e-. The data from the above analysis are, thus, not digitization noise limited and correspond to a limiting S/N of ~95/pixel.
- Percent polarization and polarization angle are derived from Q and U. Diffuse illumination differs from direct illumination in the spread in incidence angles and the bluer insolation due to Rayleigh scattering. The internal consistency of the direct and diffuse data is good, however.
- The PV panels should yield closely similar measured changes in Q and U, however, the red channel showed a greater spread than the other four channels. The reality and origin of that difference needs further confirmation.
- The dependence of the measurements on weather/wind conditions, sun angle, etc. should be measured and characterized in a thorough going program. Any natural scene is likely to be highly spatially and time dependent. The limited time for data acquisition prohibited repeating the tree data acquisition, and firm conclusions, although that is a major area of interest for the application.
- The data consistency in Figure 8 shows the independent measurements are real. The geometry of the observation (see Figure 18 in the appendix) shows specular reflection does not reach our drone, only scattering from the PV panel's surface and interior is observed. The return signal is thus due to BDRF scattering (Bidirectional Reflectance Distribution Function), or equivalently, anisotropy spectroscopy, to which we have added linear polarization to characterize the scene [17,18]. Figure 10 is a typical PV panel construction [19]. The top layer is tempered glass, which is contaminated (as in Figure 12, above) with a time-variable scattering layer on the panel surface. Below, we have the MAR-coated silicon PV cells with non-specular electrical contacts. The silicon layer is typically100 to 200 µm thick, and effectively absorbs the incident insolation between 450 nm and 1100 nm, as transmitted by the MAR layer. The nominal MAR reflectance is shown in Figure 4. The insolation is partly converted to electrons (%quantum and collection efficiency) into the

conduction band, but primarily to heat. The reflectance can be represented by end members and treated as a radiative transfer problem, e.g. as described in Berk et al. [20]. Clearly, continued, more detailed measurements than we obtained in two flights are required. The drone is, demonstrably, a nearly ideal, effective, and low cost means of acquiring the data, since sampling at a range of angles and spatial resolution is straightforward with the small, mobile drones under GPS control.

Trees (before and after leaf growth) present a more complex analysis problem. The natural scene also requires more extensive observations supported by laboratory calibrations. A nominal leaf structure, Berdnik and Mukhamed'yarov, is depicted in Figure 11. Plant canopies can be subjected to MPI analysis using radiative transfer computation characterizing the scattering and absorption by leaves [17].

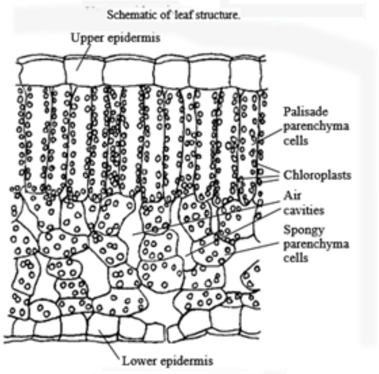

Optics and Spectroscopy, Vol. 90, No. 4, 2001, pp. 580–591.

Figure 11: Nominal Structure of a Leaf.

It is essential that relevant structures be characterized via hyperspectroscopy in the laboratory. An example is shown in Figure 15a (unpublished research, W.H. Smith, hyperspectral cellular level data).

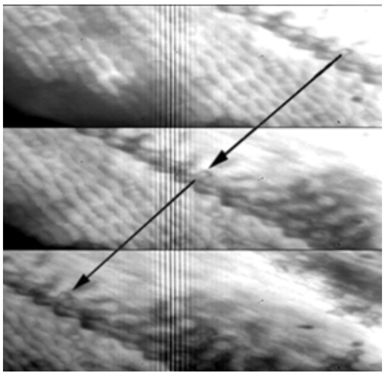

Figure 12: Pushbroom Hyperspectral Image of a Rose Petal Resolved at a Cellular Level.

These images are elements of a pushbroom scan using an imaging polarization interferometer. The black arrow indicates the same area of images as it scans through the field of vie (FOV). Both reflectance and transmission data have been obtained. From these data, the 400-1100 nm spectral content of the scene is resolved at the cellular level. With time resolved hyperspectral images, further analysis such as the time derivative of the red edge position can be extracted, as shown in Figure 15b. The stress applied was a 'drought' induced by salt injection to wheat growing in an hydroponic chamber (Bubenheim and Smith, unpublished research). The laboratory capabilities have awaited corresponding field measurement capabilities which have now evolved via drones with polarimetric hyperspectral imagers.

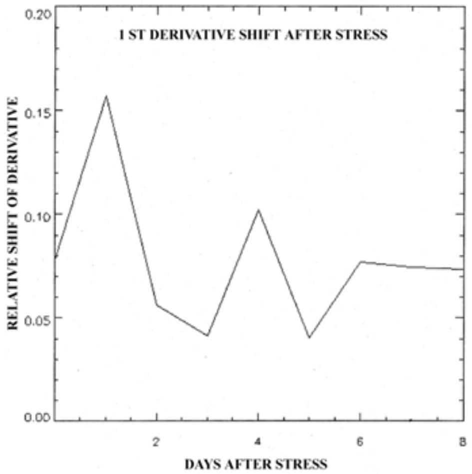

Figure 13: Time Derivative of Red Edge Shift Following Stress.

Conclusions

The P4 drone was designed for the simpler task of NDVI and NDRE measurement as a plug and play application. A drone designed for MPI should include a gimbal with rotational capability, or better yet, with snapshot MPI measurement capability, which would speed up and improve the angular accuracy of the measurements. The P4 drone CMOS detectors were not optimal for an MPI application. A well depth of only 10K e^- is marginal for MPI applications. The inaccurate image registration among the cameras, although correctable, causes a substantial wastage of pixels not overlapping in mutual FOVs. The Bayer filter camera has little scientific value. Color images can be reconstructed, if desired, from the RGB (or hyperspectral images). The image aberrations reflect the simple aspheric optics. Improved optics could render the distortion corrections unnecessary and would improve the photometric accuracy. Looking ahead, hyperspectral polarimetry (HSP) is clearly feasible, and even essential, now that we have shown that the small drones can provide a platform for MPI. HSP is in some aspects more readily performed, and remains within the data handling capabilities of small drones. The range of application is very extensive.

Patents

Author Contributions: Conceptualization, C.O. and W.S.; methodology, W.S.; software, C.O. and Y.Z.; validation, W.S.; formal analysis, W.S. and C.O.; investigation, C.O.; resources, W.S.; data curation, W.W.; writing—original draft preparation, W.S.; writing—review and editing, C.O.; visualization, C.O.; supervision, W.S.; project administration, W.S.; funding acquisition, W.S. All authors have read and agreed to the published version of the manuscript.

Funding: A summer internship for CO was funded by the McDonnell Center for the Space Sciences. The Department of Earth Environment and Planetary Science funded the flights for Course EEPS 410 in the 2024 spring term. The polarizer was provided by WHS from private resources.

Data Availability Statement: The raw data used in these analyses is placed on WUSTL Box and can be downloaded in its entirety by accessing the link. There is no limit placed on subsequent use of the data by interested parties, provided its source is acknowledged.

Acknowledgments: We wish to thank Washington University for the permission to perform these measurements over the campus/Tisch Park, and the aid of the engineering department in providing the output data shown in Figure 10.

Conflicts of Interest: The authors declare no conflicts of interest.

References

1. P4 Multispectral User Manual v1.4 EN http://www.dji.com/p4-multispectral; https://www.dji.com/mavic/info.
2. Landsat 9 Instruments: OLI-2 Relative Spectral Response https://landsat.gsfc.nasa.gov/satellites/landsat-9/landsat-9-instruments/oli-2-design/oli-2-relative-spectral-response/.
3. Barnes EM, Clarke TR, Richards SE (2000) Coincident Detection of Crop Water Stress, Nitrogen Status and Canopy Density Using Ground Based Multispectral Data. In Proceedings of the Fifth International Conference on Precision Agriculture, Madison 16-19.
4. Princeton Study: Big, Affordable Effort Needed for America to Reach Net-Zero Emissions by 2050. https://www.princeton.edu/news/2020/12/15/big-affordable-effort-needed-america-reach-net-zero-emissions-2050-princeton-study.
5. Shockley W, Queisser HJ (1961) Detailed Balance Limit of Efficiency of p-n Junction Solar Cells. J. Appl. Phys 32: 510-519.
6. Hirst LC, Ekins-Daukes NJ (2011) Fundamental Losses in Solar Cells. Prog. Photovolt. Res. Appl 19: 286-293.
7. Efficiency: Collection Probability https://www.pveducation.org/pvcdrom/solar-cell-operation/collection-probability.
8. Canadian Solar, Inc. HiDM CS1H-335W https://www.canadiansolar.com.
9. Utility Scale PV Efficiency Limit. https://www.nrel.gov/pv/cell-efficiency.
10. Bifacial Solar Cells. https://en.wikipedia.org/wiki/Bifacial_solar_cells.
11. The Desert Solar Challenge: NOMADD. https://www.nomaddesertsolar.com.
12. Solar Star Fact Sheet. https://www.bherenewables.com/include/pdf/fact_sheet_solar_star.pdf.
13. Annual Days of Sunshine in Missouri https://www.currentresults.com/Weather/Missouri/annual-days-of-sunshine.php.
14. Crouch NMA, Lynch VM, Clarke JA (2020) A Novel Approach to Quantifying Avian Mortality Rates. J. Ornithol 161: 17-24.
15. Stokes GG (2022) On the Intensity of the Light Reflected from or Transmitted through a Pile of Plates. Appl. Sci 12: 66-13.
16. Al Montazer M, Uzum (2021) A Structural Analysis of Photovoltaic Systems under Desert Con-di-tions. Res. Eng. Struct. Mat 7: 539-550.
17. Berk A, Anderson GP, Acharya PK, MODTRAN (1999) Radiative Transfer Modeling for Remote Sensing. In Proceedings of the AVIRIS Workshop, Pasadena, CA, USA.
18. Weightman P, Anderson J, Smith K (2005) advances

in Plasma Physics. Rep. Prog. Phys 68: 1251-1300.

19. Solar Panel Components and Construction-https://www.cleanenergyreviews.info/blog/solar-panel-components-construction.
20. Berdnik V, Mukhamed'yarov R (2001) Optical Properties of Thin Films. Opt. Spectrosc 90: 580-591.
21. Zhu S, Zhang J, Wang D, Ding R (2025) Efficiency Optimization in Perovskite Solar Cells. AIP Adv 15: 015-036.